Experimental and numerical investigations of a 5 A-class cathode with a LaB_6 flat disk emitter in the 2 A-20 A current range

IEPC-2017-486

Presented at the 35th International Electric Propulsion Conference
Georgia Institute of Technology – Atlanta, Georgia – USA
October 8–12, 2017

R. Joussot[1,*], G. Sary[2,†], L. Grimaud[1,‡], L. Garrigues[2,§], S. Mazouffre[1,¶], B. Laurent[3,‖],
C. Boniface[4,**], S. Oriol[5,††], F. Masson[5,‡‡]

[1]*ICARE, CNRS,*
1C avenue de la Recherche Scientifique, CS 50060, F-45071 Orléans cedex 2, France

[2]*LAPLACE, Université de Toulouse, CNRS, INPT, UPS,*
118 route de Narbonne, F-31062 Toulouse cedex 9, France

[3]*Safran Aircraft Engines, MHEF | MH, Campus de l'espace, Parc technologique*
1 avenue Hubert Curien, CS 30802, F-27207 Vernon cedex, France

[4]*CNES, Service Propulsion, Pyrotechnique et Aérothermodynamique*
18 avenue Edouard Belin, 31401 Toulouse cedex 9, France

[5]*CNES, Direction des Lanceurs,*
52 rue Jacques Hillairet, 75612 Paris cedex, France

Emissive cathodes are used as electron sources to ignite the discharge and neutralize the ion beam in Hall thrusters. In this paper, we report numerical and experimental works on a laboratory cathode for currents varying between 2 A and 20 A. The cathode design used in this study is based on a plane LaB_6 disk emitter placed within the cathode body, which is a tube with a small orifice. The cathode was studied in a diode configuration (*i.e.*, with a plate anode). Dedicated campaign studies of electric and temperature measurements have been performed to characterize the discharge and give temperature information during cathode operation. In parallel, a two dimensional quasi-neural fluid model of the cathode inside and near field plume has been developed. The numerical model was used to perform simulations at the same operating points than experiments. Experimental and numerical results both exhibit two regimes of the cathode working with extremely different plasma properties. The numerical results are compared to the experimental ones and are used to probe the plasma parameters inside the cathode, close to the surface of the LaB_6 insert. At low current and low temperature of emission, a mode characterized by a small luminous spot downstream of the cathode orifice has been observed. At high current and large temperature emission, a mode corresponding to the extension of the luminous zone in the plume towards the anode has been identified.

[*]Post-doctoral fellow, Electric Propulsion Team, ICARE, romain.joussot@cnrs-orleans.fr,
[†]Post-doctoral fellow, CEA, gaetan.sary@cea.fr
[‡]PhD student, Electric Propulsion Team, ICARE, lou.grimaud@cnrs-orleans.fr,
[§]Director of Research, GREPHE, LAPLACE, laurent.garrigues@laplace.univ-tlse.fr
[¶]Director of Research, Head of Electric Propulsion Team, ICARE, stephane.mazouffre@cnrs-orleans.fr
[‖]Engineer, Safran Aircraft Engines, MHEF | MH, benjamin.laurent@safrangroup.com
[**]Engineer, CNES, Service Propulsion, Pyrotechnique et Aérothermodynamique, claude.boniface@cnes.fr
[††]Engineer, CNES, Direction des Lanceurs, stephane.oriol@cnes.fr
[‡‡]Engineer, CNES, Direction des Lanceurs, frederic.masson@cnes.fr

I. Introduction

In a Hall Thruster (HT), a discharge is ignited in a crossed magnetic and electric fields configuration inside an annular ceramic channel. A device that furnishes electrons whose role is to supply electrons into the discharge channel able to generate the plasma and to neutralize the ion beam must be used. Tungsten filaments (employed in the 1960s in the context of gridded ion engines) are not suitable for actual missions since a very high power must be used to reach a temperature of the filaments high enough to extract the required electron current density.[1] Moreover, the rapid evaporation of the filaments and sputtering under ion impacts limit the lifetime of the system. The use of filaments was then limited to very low power HT for laboratory studies.[2] Filaments have been replaced by hollow cathode for efficiency and lifetime purposes.

In the literature, the term hollow cathode is also employed for a discharge where the multiplication of the electrons is linked to the pendulum effect induced by a specific electric potential shape. In the cathodes used in electric propulsion, the emission of electrons responsible for the plasma generation is related to a thermionic emission from an emitter material. In that sense, the term emissive cathode is more appropriate to define the cathode. Two classes of materials have been chosen for their capability to generate high electron current density. The so-called "oxide" emitter where a layer of oxide barium deposited on a porous matrix of tungsten reduces the work function of the material facilitating the emission of electrons and keeping a relatively low material temperature. At the surface (or in a pore), a chemical reaction is needed to activate a site to reduce the work function. One limiting factor is the lifetime of oxide barium layer under evaporation and the sputtering due to ion bombardment. A system of feeding of oxide material during the cathode operation (with additional injection of calcium oxides and alumina) has been proposed to enhance capability for oxide emitter to be used. A current density on the order of 10–15 $\mathrm{A\,cm^{-2}}$ for an emitter temperature of around 1500 K can be achieved.[1] This type of emitter has successfully been used in the neutralizer emissive cathode for the NSTAR mission.[3] Regardless the complexity of the BaO-W design, a major issue concerns the use of "pure" gas to avoid the poisoning by water or impurities that can modify the chemistry increasing the work function of the material.[4]

A crystalline material, namely the lanthanum hexaboride (LaB_6), offers the advantage to have a low work function and an emission from the bulk material. The presence of impurities is less a problem since the emission is not related to a specific chemistry at the emitter surface. Several work functions have been reported in the literature for LaB_6, depending on the measurement method, temperature range of the measurement, surface stoichiometry (La-to-B ratio), and crystal structure (single-crystal or polycrystalline emitter), to name a few factors. The typical work function value for LaB_6 is about 2.6 eV, higher than for BaO-W (< 2 eV). This higher work function value induces a higher material temperature for a same electron current density (10 $\mathrm{A\,cm^{-2}}$ for an emitter temperature of 2000 K). Another advantage of using LaB_6 is that a maximum of electron current density above 20 $\mathrm{A\,cm^{-2}}$ can be reached, while for a same electron current density, the evaporation of a BaO limits the lifetime of the oxide emitter.[4] LaB_6 emissive cathode has been extensively built and studied from currents varying between few A to 100 A in recent studies.[5–7]

In the majority of HT cathodes, regardless the emitter material, the thermionic effect is ignited with an external heater, and the emitter is then self-heated under the impact of charged particles (ions and electrons) coming from the plasma maintaining a high enough temperature to sustain a high thermionic electron emission current density.[8] The LaB_6 emissive cathode presented in this study works in the non-self heating mode, a heater is continuously used. This simplification offers the advantage of the device more suitable for laboratory studies by controlling the temperature of the emitter. The non-self heating mode offers also a simplification for modeling issues since a self-heating mode requires a coupling between the plasma and the thermal models and a detailed knowledge of all the thermal transfer between the materials that constitute the body of the cathode. In the present study, the geometry of the emitter differs from the majority of published works dedicated to HT cathodes since the electron emitter has a flat disk shape (and not a tube configuration).

The rest of the paper is organized as the following. The cathode design is described in Sect. II. The basics of the 2D plasma model are presented in Sect. III and numerical results obtained for two operating points are detailed in Sect. IV. Measurement methods and results for a large number of operating conditions are presented in Sect. V and Sect. VI, respectively. We summarize our main results in Sect. VII.

II. LaB_6 cathode design

The design of the cathode is largely inspired from a laboratory cathode used usually with the SPT-100-ML[9] in the PIVOINE-2g chamber.[10] A picture of the cathode and a schematic view of the simulation domain are presented in Fig. 1. A plane lanthanum hexaboride (sintered LaB_6) disk emitter (namely, the LaB_6 pellet) is placed within the cathode body (stainless steel), which is a tube of a diameter of 23 mm with a small orifice (4 mm in diameter). This orifice diameter allows a discharge current up to 6 A to be sustained at the nominal mass flow rate of the cathode ($0.4\,\mathrm{mg\,s^{-1}}$ of Xe).[11] The gap between the LaB_6 pellet and the cathode exit plane is 5.4 mm. The LaB_6 disk is 8 mm in diameter and with a thickness of 2 mm, and is embedded within a molybdenum support giving a nominal electron emission surface of $28.27\,\mathrm{mm}^2$. The LaB_6 element is heated with a heater filament placed downstream of the pellet (heated by Joule heating and thermal conduction) until it becomes hot enough to emit electrons by thermionic emission. Xenon gas is injected at the rear, far downstream of the LaB_6 element. Many studies on HT have been conducted with such a cathode design as illustrated by the published works of several research teams.[11–14]

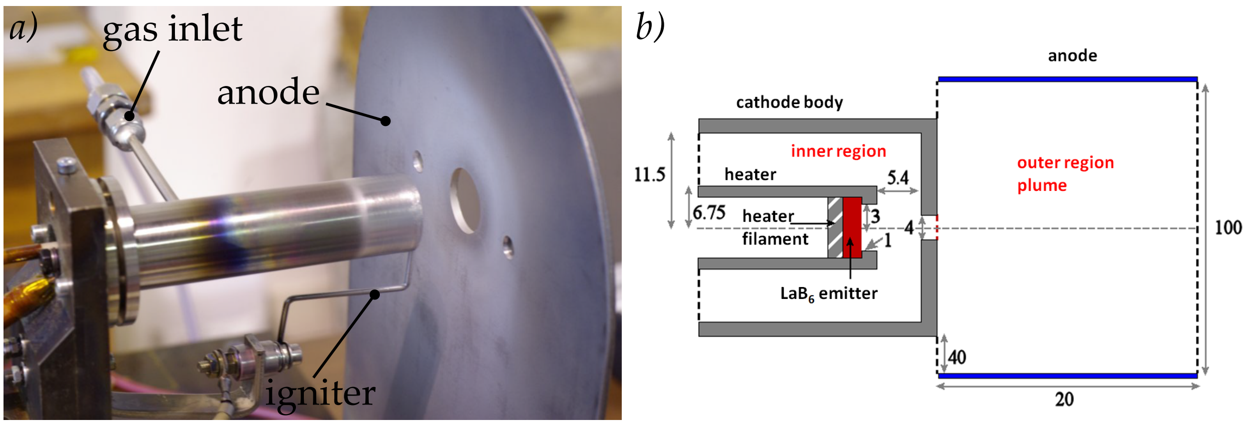

Figure 1. LaB_6 cathode: a) picture of the experimental configuration, and b) simulation domain (all the dimensions are in mm.

The cathode works in a diode configuration. A metallic flat disk in stainless steel (see Fig. 1a) with a hole in the center serves as anode and is separated from the cathode body with a gap of 20 mm. The anode is positively biased (with respect to the cathode body) to be able to extract electrons from the cathode. To ignite the discharge, a third electrode (namely the igniter, see Fig. 1a) is placed very near the cathode orifice. During the discharge, the igniter no longer works and becomes a floating electrode. In the model, a circular collecting anode is used (see Fig. 1b).

III. Overview of the 2D model

A two-dimensional fluid model of the cathode operation has been developed and validated in the context of the NASA NSTAR gridded ion engine neutralizer.[15,16] Similar approaches have also being used by Mikellides and co-workers.[17–19] In the works of Sary and co-workers,[15,16] the emitter was made in BaO and the NSTAR cathode was working in a self-heating regime, requiring a coupling between the plasma and the thermal models. As already mentioned, the LaB_6 electron emission will be controlled by an external heater. In this study, the temperature of the emitter will be given and thermal aspects not considered.

The 2D model whose the computational domain is presented in Fig. 1b is axisymmetric taking into account the inner and outer (plume) regions of the cathode. Species considered are neutrals, single charge ions, and electrons. Due to large plasma densities and low degree of ionization, a fluid approach considering Maxwellian distribution functions is considered. Transient evolution of species is retained. The electron temperature is low enough to neglect multiple charge ions. The plasma is quasineutral and specific boundary conditions will be applied to account for the sheaths (including thermionic emission, see below). Lastly, since we are not interested in the ignition of the discharge, we start the simulation with a given plasma density and with neutrals coming from a previous simulation of the established regime without plasma.

Conservation equations for neutrals and charged particles (mass, momentum, and energy) are solved.

The electric potential is calculated from the charge conservation. In the different equations, the collisional processes considered are the following: isotropic and charge exchange between ions and neutrals, Coulomb collisions between ions and electrons, and elastic and inelastic collisions between electrons and neutrals. The momentum equation for electrons is solved in the drift-diffusion approximation, where the electron mobility includes Coulomb and elastic collision frequencies and the effect of anomalous transport (see below). Additional information can be found in Ref. 15.

The calculations of ion and electron fluxes and energy losses deposited on the metallic parts of the cathode (in gray color in Fig. 1b) can be treated analytically assuming non collisional sheath knowing the plasma properties at the sheath edge[20] (plasma density, electron temperature and sheath potential drop). We assume that ions lost on the walls are recombined into neutral atoms at the temperature of the wall. A slip-length boundary conditions is used for neutrals, it consists to nullify the neutral velocity parallel to the wall on a distance below the boundary (this distance can be estimated from the fluid viscosity). The normal component of the flux is set to the recombined ion flux.

One particular attention must be put in the treatment of thermionic emission of electrons from the emitter (in red color in Fig. 1b). A dedicated model of emission has been established to be able to describe continuously the transition from a space charge limited to thermionic emission regimes that can occur in the sheath in front of the emitter. This model detailed in Ref. 15 is an extension of the work of Lin and Eng.[21] The problem is treated in one dimension between the emitting wall (grounded) at $x = 0$ and the sheath edge at a distance $x = x_0$ at a given electric potential ϕ_0. Three populations of charged species (ions and electrons coming from the bulk plasma and electrons emitted by the emitting wall, respectively at temperatures T_e and T_w) are considered. Other electron emission phenomena like secondary emission under ion/electron impacts on the emitter are neglected. By coupling analytical formulation of the density of the two populations of electron assuming Maxwellian distributions, ion density for ions in free fall, and Poisson equation, one obtains the position $x = x_b$ of the minimum of electric potential close to the wall (virtual cathode) and the electric potential drop ϕ_b that electrons must overcome to be extracted from the surface. Input parameters are the plasma density at the sheath edge n_0, electric potential drop ϕ_0, and electron temperatures T_e and T_w. The link between the emitted electron current density J_e^{em} and ϕ_b is given by the classical Richarson-Dushman law:

$$J_e^{em} = A_0 T_w^2 \exp\left(\frac{-e\phi_b}{k_B T_w}\right), \tag{1}$$

where $A_0 = 119.59\,\mathrm{A\,cm^{-2}\,K^{-2}}$ is the Richardson's constant. In the sheath model of thermionic emission, the link between ϕ_b and T_w must be specified, we have taken for the LaB_6 emitter experimental data from Lafferty:[22]

$$\phi_b\left(T_w\right) = 2.66 + 1.23 \times 10^{-4} T_w, \text{ in eV.} \tag{2}$$

In practice, we a priori calculate the emitted electron current density J_e^{em} as a function of the emission model parameters (n_0, ϕ_0, T_e, T_w) for a large range of parameter variations. During the 2D simulation, the emitted electron current density is simply extrapolated from pre-tabulated values.

At the inlet, not represented in Fig. 1b, we assume a radial profile of the neutral velocity normal to the inlet given by a Poiseuille profile. A reference density is chosen and the velocity is then computed from the desired value of the xenon mass flow injected. The temperature of the gas corresponds to the body cathode temperature. Concerning the anode plane (blue color in Fig. 1b), a uniform electron current density is assumed (whose integration gives the given electron current at the anode). Ions are accelerated at the Bohm velocity and recombined in atoms. Atoms are treated as for metallic walls. The external body of the cathode is floating and whose potential is determined through a balance of positive and negative charge current that impact on its surface. A complete description of the specific treatment of the open boundary of the plume region, which is not a physical boundary, can be found in Ref. 15.

In the NASA NSTAR cathode, the experimental evidence of fluctuating potential responsible for ion backflow on the keeper cathode has been linked to an enhanced resistivity in the cathode plume.[23] The drop of electron density induces an increase in electron velocity to maintain the desired electron current. As a result, the relative velocity between electrons and ions can exceed the ion acoustic velocity exciting the ion acoustic instability (IAI). Sary an co-workers[15] have derived a model of the acoustic instability in the context of the cathode plume (largely inspired from the works of Davidson and Krall.[24] The IAI is modeled through an energy equation and is solved for the fluctuating electric field ε_f:

$$\frac{\partial \varepsilon_f}{\partial t} + \vec{\nabla} \cdot \left(\frac{\boldsymbol{V_d}}{|\boldsymbol{V_d}|} c_{s,i} \varepsilon_f \right) = 2\gamma_M \varepsilon_f, \tag{3}$$

where $\boldsymbol{V_d} = \boldsymbol{v_e} - \boldsymbol{v_i}$ is the drift velocity and $c_{s,i} = \sqrt{(k_B T_e)/M}$ is the ion acoustic velocity and γ_M is the maximum growth rate (only the fastest mode of the maximum growth rate is retained and detailed in Ref. 15). Assuming that the Mach number $M_e = V_d / c_{s,i)} >> 1$, and $\gamma_M << \omega_{pe}$, ω_{pe} being the electron plasma frequency, we then can link the anomalous electron collision frequency to the electron temperature, plasma density, and fluctuating electric field ε_f:

$$\nu_{e,AN} = 2\sqrt{\pi}\omega_{pe} \frac{\varepsilon_f}{n k_B T_e}. \tag{4}$$

Heating terms in the energy conservation equation of ions and electrons have also been included. The system of equations here described is only valid for the description of the growth rate of the IAI in the quasi-linear regime, when ion and electron energy distribution functions are almost Maxwellian. It cannot describe the saturation mechanism of the instability due to kinetic effect. Derived from Particle-In-Cell simulations, Davidson and Krall have proposed to limit the maximum of ε_f:[24]

$$[\varepsilon_f]_{MAX} = \alpha_{nT_e} n k_B T_e, \tag{5}$$

where $\alpha_{nT_e} \in \left[10^{-3}; 10^{-2}\right]$. Results presented in Ref. 15 for a BaO NASA NSTAR cathode have shown that $\alpha_{nT_e} = 3 \times 10^{-3}$ gives a reasonable agreement with experiments. We keep the same value for this study.

IV. Numerical results

We have performed two calculations, for a low electron current ($I_e = 4.8\,\mathrm{A}$, for an emitter temperature of 1913 K) and a high electron current ($I_e = 12\,\mathrm{A}$, for an emitter temperature of 2073 K). The electron current I_e corresponds to the discharge current that was measured experimentally (see following sections). The neutral mass flow rate is fixed to $0.4\,\mathrm{mg\,s^{-1}}$ (4 sccm, standard cubic centimeter). The properties of the cathode simulated are summarized in Table 1. The emitter temperature has been fixed from the measurements of emitter temperature (see Sect. V and below). Pictures of the cathode working in these two regimes are presented in Fig. 2.

Table 1. Properties of the cathode simulated

	Low current	High current
Discharge current I_e	4.8 A	12 A
Neutral mass flow rate	$0.4\,\mathrm{mg\,s^{-1}}$	$0.4\,\mathrm{mg\,s^{-1}}$
Emitter temperature	1913 K	2073 K
Discharge mode	spot	plume

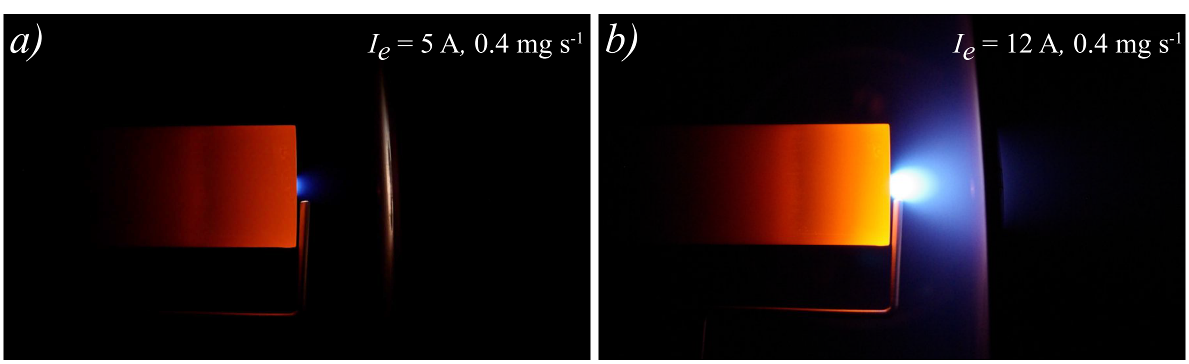

Figure 2. Pictures of the plasma discharge operated in: *a)* spot mode at $I_e = 5\,\mathrm{A}$, and *b)* plume mode at $I_e = 12\,\mathrm{A}$. The mass flow rate is $0.4\,\mathrm{mg\,s^{-1}}$ of Xe. The anode is on the right side. The exposure time is 50 ms.

A. Low discharge current $I_e = 4.8\,\mathrm{A}$

We have plotted the time averaged two dimensional profiles in axial and radial directions of the plasma and neutral densities (together with ion current field lines) in Fig. 3.

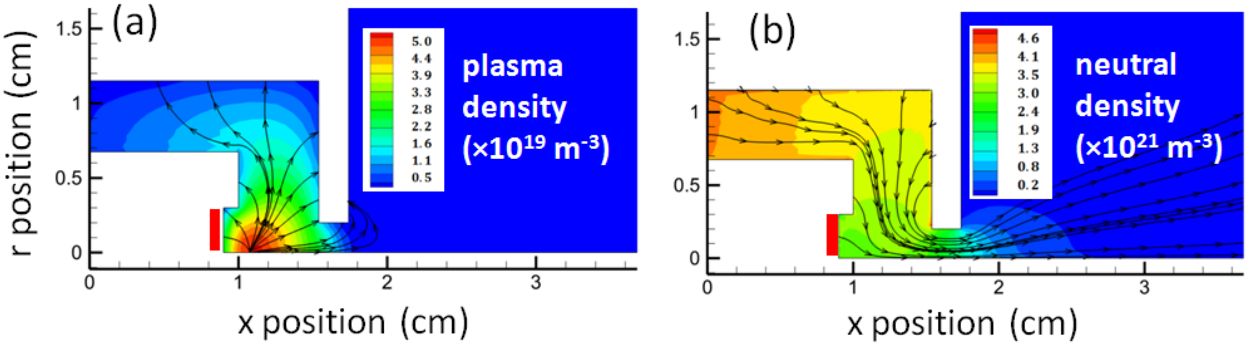

Figure 3. Two dimensional profiles of: *a)* plasma and *b)* neutral densities. The ion current field lines are also plotted. The emitter $\mathrm{LaB_6}$ disk is also represented in red. The discharge current is fixed to $I_e = 4.8\,\mathrm{A}$.

In Fig. 3a, the maximum of plasma density ($\approx 5 \times 10^{19}\,\mathrm{m^{-3}}$) occurs in a thin region immediately face to the emitter. Downstream of the cathode orifice, the plasma density sharply drops, while upstream, a non-negligible plasma density in the lateral part of the heater and cathode body exists. In the region of the maximum of plasma density, a neutral depletion is associated (see Fig. 3b). The neutral current field lines are slightly perturbed, only the ion recombination on the cathode body walls (see the ion current field lines in Fig. 3a) modifies the velocity field of the neutrals. More interesting a fraction of ion current is lost on the external part of the cathode orifice that can lead to the erosion and damage of the orifice.

The 2D profiles of plasma potential (and electron current field lines) and electron temperature are plotted in Fig. 4. The maximum of plasma potential ($\approx 18\,\mathrm{V}$) occurs close to the anode to extract electrons, as expected. We note that a local maximum of plasma potential ($\approx 17\,\mathrm{V}$) exists face to the emitter and a local minimum of plasma potential also appears in the cathode orifice. Despite the electric force, the gradients of plasma density (Fig. 3a) and electron temperature (Fig. 4b) permit to the electrons to be extracted from gradient of pressure effects. This is confirmed looking to the electron field lines in Fig. 4a. We notice that mostly all electron current field lines passing through the cathode are directed towards the orifice. That is a clear evidence that all the emitter surface contributes to the emission.

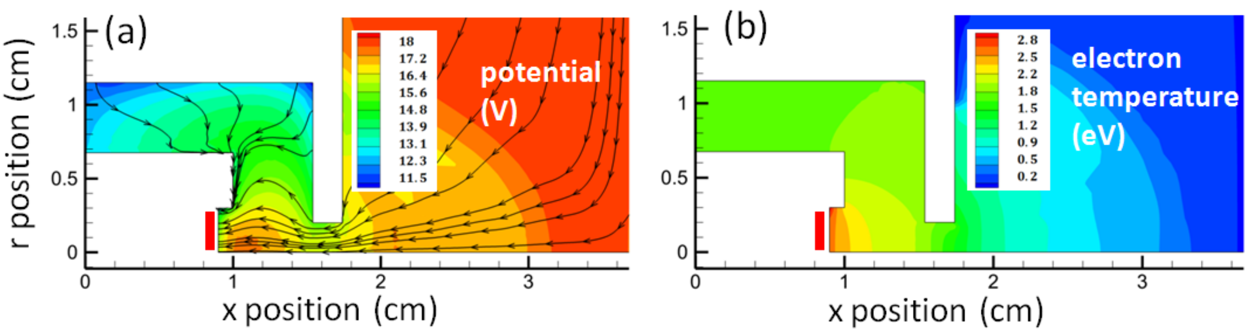

Figure 4. Two dimensional profiles of: *a)* plasma potential (and electron current field lines) and *b)* electron temperature. The emitter $\mathrm{LaB_6}$ disk is also represented in red. The discharge current is fixed to $I_e = 4.8\,\mathrm{A}$.

The maximum of electron temperature ($\approx 3\,\mathrm{eV}$) is concentrated near the emitter and it decreases rapidly downstream of the orifice (see Fig. 4b). In practice, it can be deduced that if a light emission is visible in the plume of the cathode (due to the excitation of the xenon by electron impact), it will probably be restricted to the immediate vicinity of the orifice. Qualitatively, we can associate these simulation results with the spot mode visible when the cathode operates in a low discharge current (see Fig. 2a).

We finally have plotted the two-dimensional profiles of neutral pressure and ionization source term (number of electron-ion pairs created by units of space and time) in Fig. 5. The neutral pressure whose varies from 100 Pa (at the rear of the cathode body) to 10 Pa (in the vicinity of the orifice) is smaller than the previous simulations made for a BaO emitter of the NASA NSTAR cathode[16] (≈ one order of magnitude). This can be certainly associated to a wider diameter of the orifice in the case of the cathode studied here. We observe that the ionization takes places quasi only inside the cathode body where the electron temperature and plasma and neutral densities are large. The emitted electrons from the cathode gain energy in the potential drop face to the emitter (Fig. 4a). Downstream of the orifice, the electron temperature is too low to generate a significant plasma source term. It is therefore necessary to take a certain caution of the interpretation of the cathode operation. In particular, Albarède[11] tends to associate the light emission in the external region of the cathode (and the cathode mode of operation, spot or plume) to the ionization of the xenon. Numerical results show that xenon ionization occurs almost exclusively in the internal region. The light emission immediately downstream of the orifice seen in Fig. 4a can certainly be associated to excited neutral atoms.

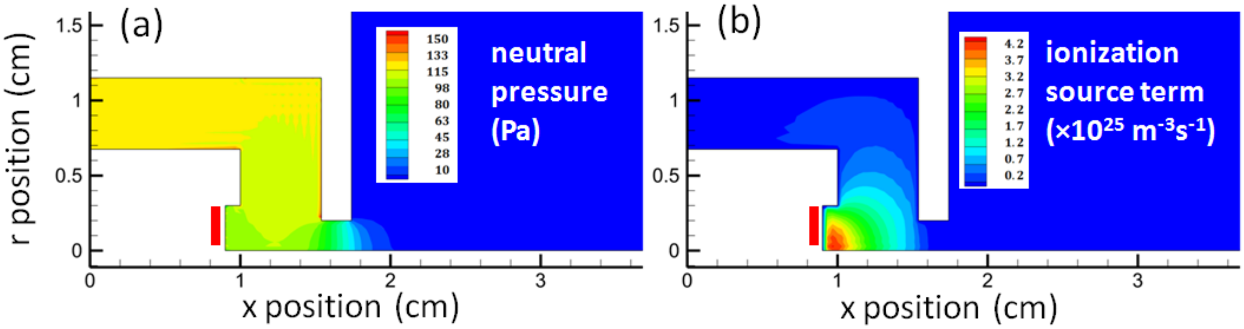

Figure 5. Two dimensional profiles of: *a)* neutral pressure and *b)* ionization source term. The emitter LaB_6 disk is also represented in red. The discharge current is fixed to $I_e = 4.8\,\mathrm{A}$.

We can make a balance of the currents. The electron current emitted at the pellet is 4.3 A. The electron current absorbed by the various metallic walls (anode excepted) amounts to 1.7 A while the absorbed ion current is 2.1 A. Since the imposed discharge current is $I_e = 4.8\,\mathrm{A}$, volume ionization must contribute to an equivalent current of 2.2 A, which differs slightly from the ionic current lost on the walls. This difference stems from the fact that the ions lost on the anode are not taken into account in this macroscopic current balance. Using the ion current lost to the walls as an estimate of the term source of ionization in volume linked to cycle ionization/recombination of the neutrals, and noting I_e^{em} and I_i^{ab} the electron emitted and ion loss currents, the contribution of the electron emission from the emitter to the total electron current is $I_e^{em}/(I_e^{em} + I_i^{ab}) \approx 67\%$. As a remark, for a discharge current $I_e = 5\,\mathrm{A}$ and a xenon mass flow of $0.36\,\mathrm{mg\,s^{-1}}$, the contribution of the electron emission from the BaO emitter in the NSTAR cathode was 75%.[16] This can be attributed to a higher temperature of the LaB_6 emitter for a same operating point.

The temperature of the emitting element is here maintained at 1913 K and the simulations do not take into account the thermal model for the cathode. It is nevertheless possible to estimate the energy fluxes produced by the plasma bombardment, in particular on the emitter surface. The emitting element gains directly 0.3 W and 3.2 W through electron and ion bombardments, respectively. It can be compared to the loss of 13.6 W for the electron emission. The electron bombardment on the other surfaces (cathode body, heater) is in fact more intense and the energy deposition for all the surfaces (emitter included) reaches 13.7 W. Now the other surfaces, and in particular the cathode external body, are not in direct thermal contact with the emitter. A supply of an external power is required to maintain a self-thermal operation of the cathode, as expected for such a type of cathode design.[8]

It is useful to plot the charged particles current density along the emitter ($r = 0$ corresponds to the cathode axis). We define the electron current density as $\boldsymbol{j_e} = -en\boldsymbol{v_e}$ and the ion current density as $\boldsymbol{j_i} = en\boldsymbol{v_i}$ (the negative electron current density is simply due to the choice in the normal direction of the vector). As we see in Fig. 6, the emission of electron current is almost uniform (it varies from $14.3\,\mathrm{A\,cm^{-2}}$ on axis to $12.8\,\mathrm{A\,cm^{-2}}$ off axis). The losses of electron and ion current densities are relatively low as a result of a low plasma density (compared to the case of a self-heated BaO emitter). The almost uniform profiles of absorbed current densities are also related to the choice in a uniform emitter temperature in the simulations.

We have also calculated an effective work function at the emitter surface (that includes the Schottky effect and space charge limitation); it is almost uniform and equal to 2.84 eV. For comparison, the work function under of the solely effect of temperature, calculated with Eq. (1), is $\approx 2.9\,\mathrm{eV}$. Since the presence of plasma leads everywhere to a reduction in the effective work function with respect to its dependence as a function of temperature (through the Schottky effect), we can conclude that the plasma is sufficiently dense over the whole surface of the emitter to extract the emitted electron current. This is corroborated indirectly by the electron current lines which originate over the entire surface of the emitting pellet (see Fig. 4a). For the discharge current required in this simulation case ($I_e = 4.8\,\mathrm{A}$), the surface of the pellet is therefore well dimensioned. The emitted current density, everywhere less than $20\,\mathrm{A\,cm^{-2}}$ (see Fig. 6), also guarantees a slow evaporation of the LaB_6 emitter. We recall that this current density of $20\,\mathrm{A\,cm^{-2}}$ is often taken as the upper limit of the operating modes in which the evaporation of the LaB_6 emitter would be slower than a BaO type emitter for the same emission current.[5] The simulated plasma potential (of the order of 18 V) is however large, which may lead to an accelerated erosion of the emitter by ion impact.

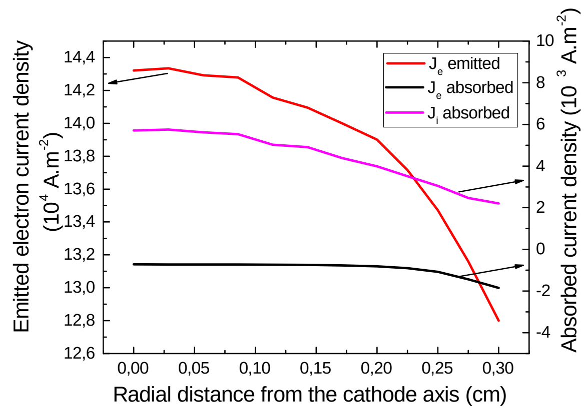

Figure 6. Electron (J_e) and ion (J_i) current densities calculated at the emitter surface. The discharge current is fixed to $I_e = 4.8\,\mathrm{A}$.

B. High discharge current $I_e = 12\,\mathrm{A}$

We have plotted in Figs. 7 and 8 the averaged 2D profiles of plasma and neutral densities, potential and electron temperature for a discharge current of $I_e = 12\,\mathrm{A}$. As for $I_e = 4.8\,\mathrm{A}$, the plasma takes place quasi only inside the cathode. The neutral profile looks like to the previous case. The orders of magnitude of densities are also very similar. Increasing the discharge current leads to modify the profile of electron temperature as we see in Fig. 8b, induced by a higher discharge potential (32 V compared to 18 V in the previous case). The maximum of electron temperature is now located at the cathode exhaust. We attend to observe a higher light emission upstream of the cathode orifice and make a link with the plume mode observed in Fig. 2b. The higher electron temperature in the plume is related to the IAI that induces a higher resistivity and potential in the plume. Ions created in the plume are directed towards the cathode (see one example of ion current line plotted in Fig. 7a), leading to potential erosion of the cathode body.

We have plotted in Fig. 9a the time variation of the electric potential at the anode. The electric potential strongly oscillates ($\pm 15\,\mathrm{V}$ from a mean value of 31.1 V) at a frequency of 50 kHz. For a same cathode operation, fluctuations of electric potential have been measured at a frequency (65 kHz, see Sect. VI). In the spectrum, we also see a higher frequency that appears and disappears periodically (not shown here). The low frequency is associated to the ion acoustic velocity, while the high frequency is the result of the competition between electron heating due to IAI and Landau damping.[15,16] The time evolution of plasma and fluctuation densities on axis at 5 mm downstream of the cathode orifice are presented in Fig. 9b. The fluctuation density has been normalized to the maximum threshold of density fluctuations (α_{nT_e}). We notice that the peaks of plasma density are correlated to the collapse of the instability (normalized fluctuation densities tend to 0) and the disappearance of the high frequency component. When the plasma density is almost constant in time ($\approx 3 \times 10^{17}\,\mathrm{m^{-3}}$), the density of fluctuations increases again to reach a threshold value of 3 and the fluctuations of electric potential and temperature at high frequency start again. When the instability is "on", the electron heating generates more electron-ion pairs in the plume leading to an increase in plasma density. The increase in plasma density induces a reduction in the electron drift velocity that

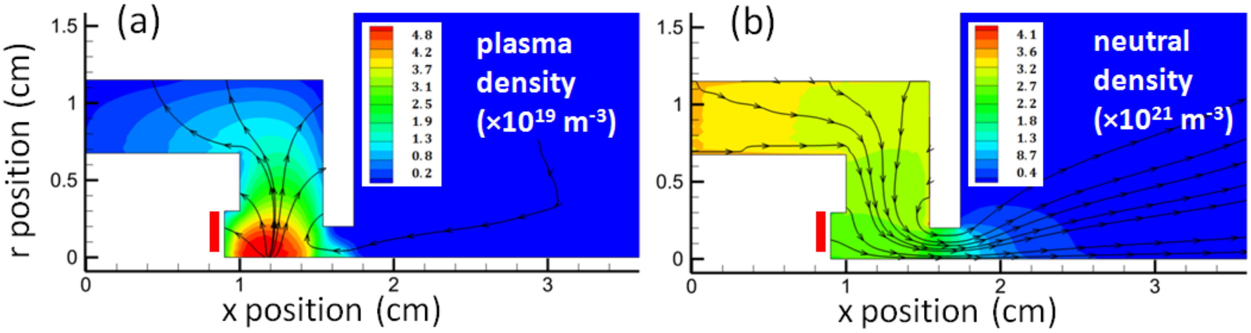

Figure 7. Two dimensional profiles of: *a)* plasma and *b)* neutral densities. The current field lines are also plotted. The emitter LaB$_6$ disk is also represented in red. The discharge current is fixed to $I_e = 12\,\mathrm{A}$.

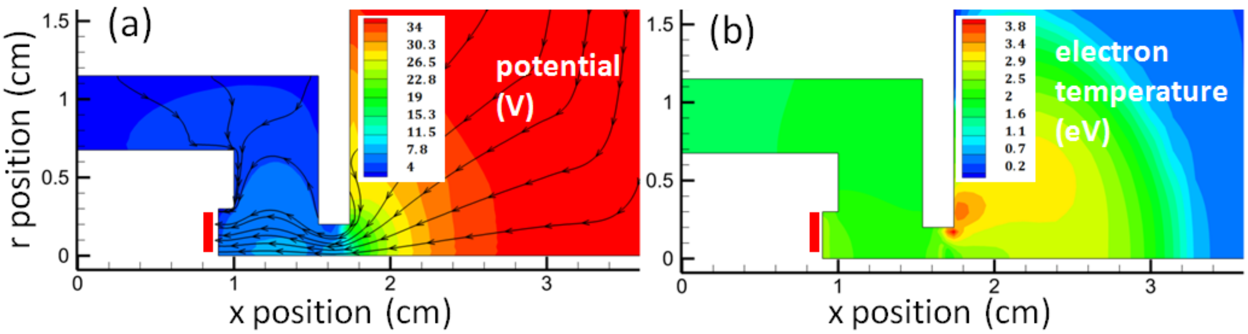

Figure 8. Two dimensional profiles of: *a)* plasma potential (and electron current field lines) and *b)* electron temperature. The emitter LaB$_6$ disk is also represented in red. The discharge current is fixed to $I_e = 12\,\mathrm{A}$.

becomes much smaller than the IAI threshold. The associated fluctuations of plasma properties disappear, the electron temperature and density decrease. When the plasma density is sufficiently low (and the electron drift velocity high enough), the instability appears again.

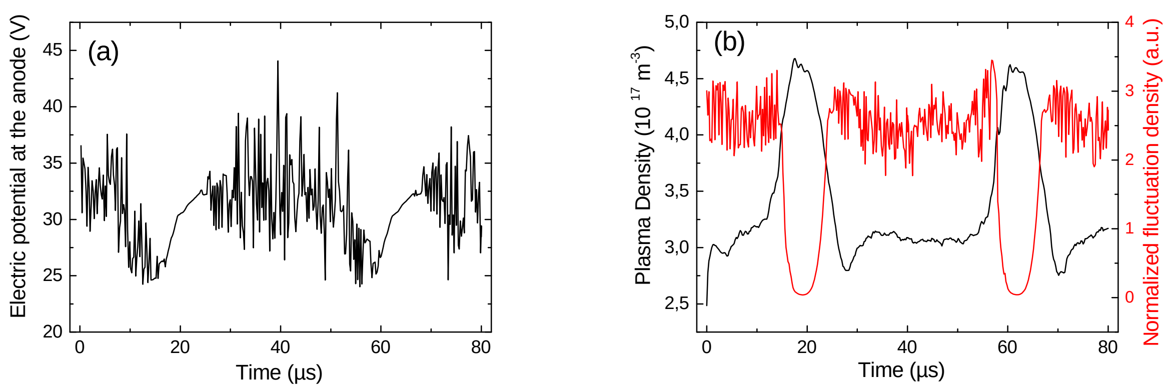

Figure 9. Time variation of: *a)* electric potential and *b)* plasma and fluctuation densities. The discharge current is fixed to $I_e = 12\,\mathrm{A}$.

The consequence of the IAI is the generation of high enough energetic ions that can bombard and erode the cathode body. The maximum of kinetic energy of the ions impacting the cathode body (lateral wall face to the plume) is 41 eV (and 28 eV in average). For comparisons, in the case of the low discharge current, the maximum kinetic energy was 8.9 eV (and 7.3 eV in average). Clearly, the cathode operation at high discharge current leads to an erosion of the lateral wall of the cathode face to the plume. In the plume mode, experimental evidence of accelerated erosion has been observed.

Very long simulations (hundreds of μs) sometimes (depending of initial conditions) have shown a stabilization of the discharge. The instability was always saturated in the near field plume of the cathode. The time variation of the plasma density was then almost constant and the electric potential at the anode was stabilized around 35 V. A signature of an unstable regime is visible since very small fluctuations (few percent of the averaged values) of plasma properties inside the cathode were present. A small modification of the temperature of the emitter (2053 K instead of 2073 K) destabilizes the discharge and similar fluctuations of plasma properties as shown here are again observed. An increase in the temperature of the emitter (2100 K) also produces a similar behavior.

Experimentally, the discharge potential measured for the operating point studied here is on the order of 35 V (see Sect. VI), while the simulated discharge potential is around 31 V. It will be recalled that the model accurately predicts (in comparison with the experimental measurements) a discharge potential in the case of a low current of the order of 18 V. An increase in the cathode discharge potential in the case of a higher current can be attributed physically to the penetration of the cathode and the triggering of the acoustic instability downstream of the orifice.

In the case $I_e = 12\,\mathrm{A}$, the model simulates a floating potential of the external body close to $-1.5\,\mathrm{V}$, while the measured one is 7 V. It is surprising that the potential of the floating body decreases sharply when the discharge current is increased (the floating potential of the cathode body was around 8 V when $I_e = 4.8\,\mathrm{A}$). Experimentally, however, it was observed that the floating potential of the external body was relatively insensitive to the discharge current over the range $[5\,\mathrm{A} - 20\,\mathrm{A}]$ studied. However, in the case $I_e = 12\,\mathrm{A}$, the simulation results seem physically justified: with the increase in electron heating in the plume, the voltage drop in the sheath facing the floating cathode body must increase to limit the electron collection from the plasma. Perhaps the too large potential drop between low and high current cases can be attributed to the "simplistic" fluid description of the plasma and the acoustic instability in the cathode plume. In particular, the presence in the case of $I_e = 12\,\mathrm{A}$ a peak of electron temperature close to the external face of the cathode (see Fig. 8b) whose physical reality can be discussed. Even limited to a restricted region close to the cathode orifice, the local maximum of the electron temperature obtained in the calculations is likely to greatly increase the electron current collected at the wall of the floating external body and thus to cause a potential drop.

If we pay attention to the current balance, we find that for a discharge current imposed at the cathode of 12 A, the current emitted by the pellet is 13.3 A. The electron and ion currents lost at the walls are 3.2 A and 1.8 A, respectively. In contrast to the case $I_e = 4.8\,\mathrm{A}$, it can be seen that the pellet now delivers an emission current greater than the discharge current. When $I_e = 12\,\mathrm{A}$, the electron emission contributes to 88% of the total equivalent electron current (including ionization in volume). Concerning the energy balance, the electron emission causes an energy loss of 43.4 W. This loss is only partly compensated by the ion and electron bombardments on the pellet, which respectively provide 2 W and 10 W. Thus, in this mode of operation, the operation of the cathode is also not self-heating and an additional heating is necessary.

The ion current density collected at the surface of the emitting pellet is similar to the simulation case at low discharge current (Fig. 6) and counts for a total of 0.11 A. The maximum ionic current density is $5 \times 10^3\,\mathrm{A\,m^{-2}}$. In the case of $I_e = 12\,\mathrm{A}$, the electron current density absorbed on the surface of the pellet is much higher than in the case $I_e = 4.8\,\mathrm{A}$ and its maximum reaches $4.5 \times 10^4\,\mathrm{A\,m^{-2}}$. This is due to a lower potential (8.7 V compared to 18 V) in the case of a higher discharge current (since the plasma density at the sheath edge is almost the same in the two cases $\approx 2 \times 10^{19}\,\mathrm{m^{-3}}$).

We have finally plotted the radial variation of emitted electron current density and effective work function in Fig. 10. As for the case of a lower discharge current, the emission current density is higher in the center of the pellet than on its edge (here twice as intense). The decrease in the emission current density at the edge is related to the increase in the effective work function and the insufficient density of the plasma to carry the current. The experimentally measured value, from Eq. (2), of the material work function for at 2073 K (in the limit of sufficiently dense plasma with a zero sheath potential) is reported by a horizontal dashed line in Fig. 10. This value can be compared to the effective work function obtained in the calculations. If the central region of the pellet takes advantage of the presence of the plasma on its surface and thus of the Schottky effect which increases the emission current density, this is not the case for the edge of the pellet (the effective work function increases beyond the experimentally measured value, from Eq. (2)). Thus, the plasma at the edge of the pellet (yet of reduced size) is not sufficiently dense to extract the emitted current and the emitter is subjected to a space charge saturation regime. However, we can moderate the scope of this remark by noting that the uniform temperature distribution of the emitter is idealized. By taking a more realistic account of a decrease in the temperature of the pellet on its edge, it is probable that the current density emitted at the edge of the pellet is smaller and therefore closer to that of the plasma can transport.

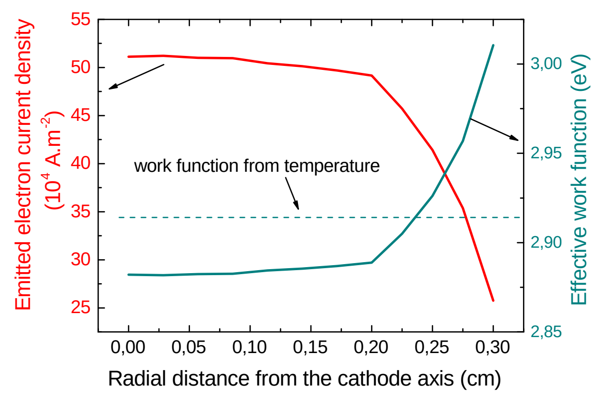

Figure 10. Emitted electron current density and effective work function calculated at the emitter surface. The discharge current is fixed to $I_e = 12\,\mathrm{A}$.

From a practical point of view, the simulation case $I_e = 12\,\mathrm{A}$ shows that this pellet geometry is not appropriate: the increase in the discharge current is accompanied by a reduction of the useful surface of the pellet. It is plausible that a narrower orifice of the cathode may contribute to increase the gas pressure in the cathode (it is only 130 Pa upstream of the simulation domain) and thus allowing the generation of a denser plasma in front of the emitter able to facilitate the extraction of the emitted current.

V. Measurement methods

A. The NExET test bench

Experiments were performed in the NExET (New Experiments on Electric Thrusters) vacuum vessel (Fig. 11). This test bench was commissioned at the ICARE laboratory in November 2008 and is used in conjunction with the PIVOINE-2g chamber[10] to carry out experiments in the field of electric propulsion. The NExET test-bench is a stainless steel chamber, 1.8 m in length and 0.8 m in diameter. It is equipped with a pump stack composed of a large dry pump, a $350\,\mathrm{L\,s^{-1}}$ turbomolecular pump to evacuate light gases down to 10^{-6} mbar-N_2, and a cryogenic pump with a typical surface temperature of 25-35 K (with a pumping speed of $8000\,\mathrm{L\,s^{-1}}$) to absorb gases such as Xe and Kr. A large water-cooled screen covered with graphite tiles is mounted at the back of the chamber. It absorbs part of the ion beam energy therefore reducing the thermal load onto the cryogenic surface. A background pressure of 2×10^{-5} mbar-Xe is achieved inside the chamber with $1\,\mathrm{mg\,s^{-1}}$ xenon gas flow rate and 250 W input power. The heavy particle momentum exchange mean free path is, in this pressure condition, of the order of the chamber length, which warrants a negligible impact of the residual gas. The chamber is equipped with several observation windows, portholes and diagnostic ports. The interior of the facility is easy to access thanks to a large door located on the front side.

B. Instrumentation

1. Electrical measurements

The experiment was set up in a diode configuration. The heater was connected to a Midec power supply (SK 40-25, 40 V, 25 A). The anode was connected to an Elektro-Automatik power supply (EA-PSI 9200-70, 200 V, 70 A, 5 kW). The cathode base was grounded and the external body of the cathode was floating. Anode and heater voltages were measured using Tektronix voltage probes (P6139A, 500 MHz, 8.0 pF). The discharge current (*i.e.*, the anode current) was measured using a Tektronix current probe (TCP202, dc to 50 MHz bandwidth). Probes were connected to a Tektronix digital oscilloscope (TDS5104, 1 GHz, $5\,\mathrm{GS\,s^{-1}}$)

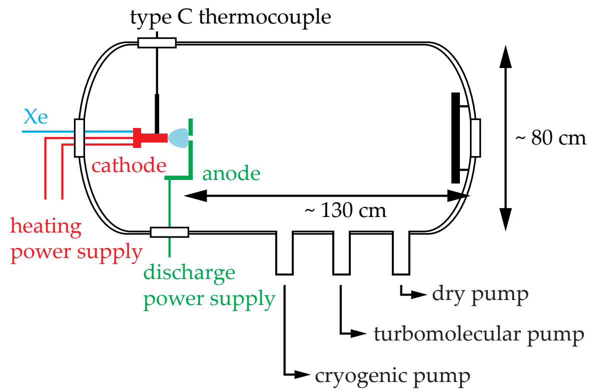

Figure 11. Schematic of the NExET vacuum vessel with the cathode installed inside.

to monitor and record the electrical signals at a sampling rate of 1 MHz.

2. Temperature measurements by thermocouples

Thermocouple measurements have proven to be challenging in LaB_6 cathodes because of the high temperatures of the electron-emitting insert and limited access to the cathode interior.[25] The very limited number of published papers shows the difficulty of measuring the emitting insert temperature during the cathode operation, although the LaB_6 insert temperature is one of the most important parameters to estimate its lifetime,[22] which directly impacts the cathode lifetime. To the authors' knowledge, only one study from the Jet Propulsion Laboratory (U.S.A.) presents a complete and detailed investigation of the direct measurement of the emitter temperature of a LaB_6 cathode used as electron source for HTs.[25] For BaO-W inserts, more studies have been published on direct temperature measurements of the insert,[26,27] since in this case the temperature is lower.

A metal sheathed mineral insulated (MSMI) type C (W5%Re/W26%Re) tungsten-rhenium thermocouple (Thermocoax) was employed to measure the LaB_6 emitter temperature during the cathode operation. The type C thermocouple was routed into the cathode through a small hole in the external body and inserted in a small hole in the pellet holder, allowing the thermocouple to be in direct contact with the LaB_6 insert.[28] To maintain this direct contact during the experiments, the type C thermocouple was mounted above the cathode in a downward direction and was fixed loosely to its support. The thermocouple was therefore lightly leaned on the insert lateral wall. Alumina tubes were employed to avoid short circuits between the external body of the cathode (floating) and the LaB_6 pellet (grounded). Additional thermocouples were used to monitor the temperature at several locations where temperatures were lower. MSMI type N thermocouples secured with tungsten foils were employed to measure the temperature of the external body of the cathode, the cathode flange, the igniter, and the rear side of the anode. All the thermocouples are connected to PID temperature controllers (P.M.A, ECO 24) and signals were read and recorded by a computer at a sampling rate of 1 Hz.

VI. Experimental results

A. Operating envelope

Once the heating phase of the LaB_6 emitter has been achieved (see Ref. 28 for further details), the discharge is ignited by applying a positive potential to the igniter. As soon as the plasma is present downstream of the cathode orifice, the ignition potential is applied to the anode and the igniter is allowed to float. Because the power supply of the discharge is used in a current-controlled configuration, the anode potential is free to vary and adapts to experimental configurations (*i.e.*, cathode design, mass flow rate, discharge current, etc.). During cathode operation, the heating power is maintained at about 185 W to ensure that the cathode does not switch off during experiments at low discharge current.

Figure 12 shows the anode potential V_a versus the discharge current I_e, for three mass flow rates of xenon

($0.2\,\mathrm{mg\,s^{-1}}$, $0.4\,\mathrm{mg\,s^{-1}}$, and $0.6\,\mathrm{mg\,s^{-1}}$). Each value of the two electrical parameters V_a and I_e is obtained by averaging several oscilloscope traces. The record length of each time series is set to ensure a sufficiently high sampling frequency in order to provide an adequate cut-off frequency (500 kHz). After each increase in the current discharge, a waiting time of 600 s is applied to ensure a steady state of heat transfer inside the cathode. During each run, the value of the current discharge is kept unchanged. The errors bars in Fig. 12 correspond to the total uncertainties.[28]

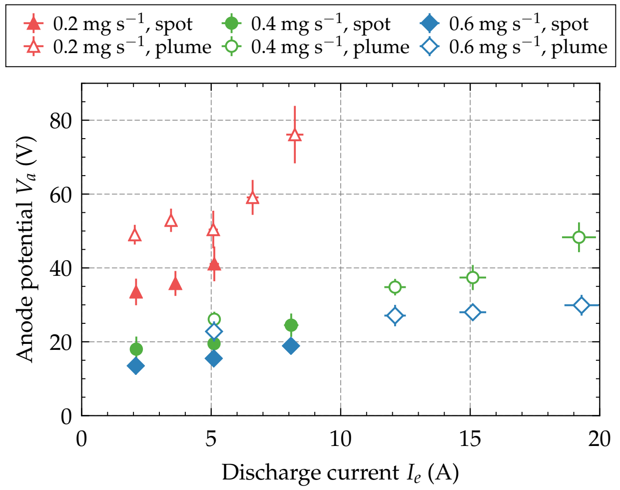

Figure 12. Anode potential V_a according to the discharge current I_e for different mass flow rates of Xe. Closed and open symbols stand for spot mode and plume mode, respectively.

Two discharge regimes are reported in Fig. 12: the spot mode and the plume mode. Both working regimes of such a cathode in diode configuration are well known and described in the literature.[29,30] At a given mass flow rate, the working regime of the discharge changes when the current is progressively increased. The spot-to-plume transition is characterized by an increase in the average value of the anode voltage V_a of about 10 V, V_a being lower in the spot mode.[31] The occurrence of a spot-to-plume transition when the discharge current increases is not contradictory with the literature, though this behavior was not reported frequently in studies on HT cathodes operated in diode configuration. Several teams have indeed reported this behavior for different cathode designs and ranges of discharge current.[32,33] For a given value of I_e, it is possible to observe both regimes (not simultaneously) because there is a hysteresis.[34] Depending on how the discharge current is modified, positive ramp or negative ramp, the discharge can be operated in spot mode or in plume mode.

For this cathode design, the mass flow rate of $0.2\,\mathrm{mg\,s^{-1}}$ is critical to run the cathode in spot mode, since the plume mode is easily promoted whatever the discharge current is. In addition, high and fast-growing values of V_a are measured when I_e is increased. In order to avoid very high values of V_a being reached, the discharge current is limited to 8 A when the mass flow rate is set to $0.2\,\mathrm{mg\,s^{-1}}$ of Xe. Higher values of the Xe mass flow rate allow the discharge to be operated in spot mode. Both mass flow rates of $0.4\,\mathrm{mg\,s^{-1}}$ and $0.6\,\mathrm{mg\,s^{-1}}$ of Xe show similar trends: V_a rises when I_d increases and the plume mode is promoted if $I_e \geq 8\,\mathrm{A}$. The fact that similar trends are observed for different mass flow rates is expected with such a cathode setup, in particular when the cathode is operated in spot mode.[8] For these two mass flow rates ($0.4\,\mathrm{mg\,s^{-1}}$ and $0.6\,\mathrm{mg\,s^{-1}}$), the plume mode at $I_e = 5\,\mathrm{A}$ is obtained with a negative current ramp. In these experiments, the mass flow rates of $0.4\,\mathrm{mg\,s^{-1}}$ and $0.6\,\mathrm{mg\,s^{-1}}$ of Xe are too low to ensure that the cathode will operate in spot mode if the discharge current is higher than 8 A.

B. Discharge modes

The classical discharge morphology of a cathode running either in spot mode or in plume mode is shown in Fig. 2. The spot mode is characterized by a small luminous spot observed just downstream of the cathode orifice.[8] This contrasts with the bright diverging plume that extends downstream of the cathode and beyond the anode in the case of plume mode. Even though the visual morphology of the discharge can be used as a possible tool to determine what the discharge regime is, it is more relevant to study the standard deviation of the electrical parameters in order to determine the discharge mode beyond any doubt.[28] Visual determination of the discharge regime can be tricky in some cases because other discharge modes with similar features to those of the plume mode can be observed.[35] In spot mode, fluctuations of the electrical parameters are very low, about 2% of the average value. This contrasts to the plume mode where the amplitude of the current fluctuations corresponds roughly to 10-30% of I_e.

The time traces plotted in Fig. 13a illustrate the different behaviors of the discharge current. As expected, the spot mode ($I_e = 5\,\mathrm{A}$) exhibits a very low level of fluctuations. By increasing the discharge current (at constant mass flow rate), the discharge regime changes into the plume mode ($I_e = 12\,\mathrm{A}$). The power spectral density of the current discharge is estimated from the time traces in order to determine the main frequencies of the current oscillations. Welch's method is used to plot the power spectra. This method is used because it reduces noise in comparison with the standard periodogram spectral estimating method.

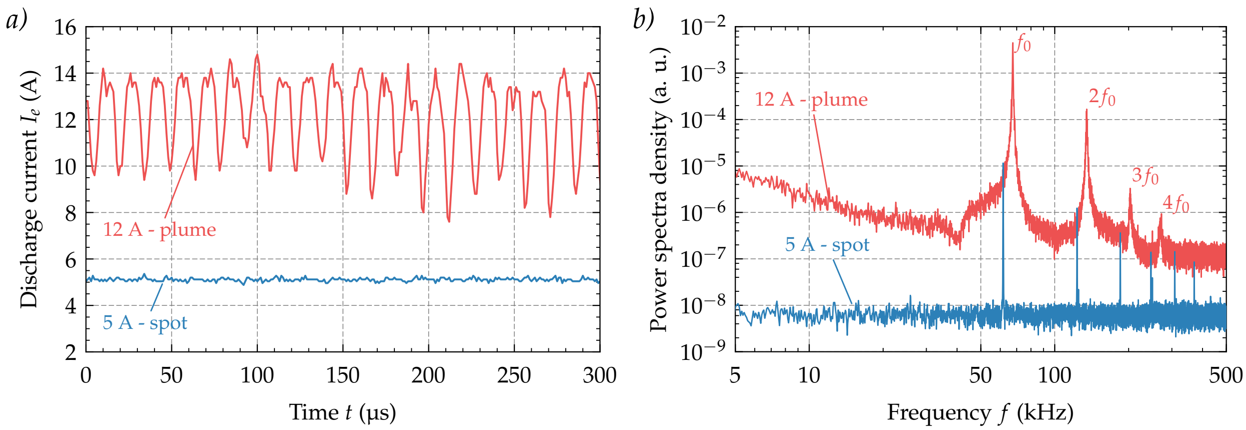

Figure 13. Discharge modes: *a)* time series of the discharge current, and *b)* power spectral density of I_e according to the discharge current. The mass flow rate is $0.4\,\mathrm{mg\,s^{-1}}$ of Xe.

Figure 13b shows the power spectra of the time traces plotted in Fig. 13a. The power spectrum corresponding to the spot mode ($I_e = 5\,\mathrm{A}$) is obviously less energetic,[36] since a very low level of fluctuations was measured. However, one can observe a very narrow peak at $f_0 = 62.7\,\mathrm{kHz}$ with its associated harmonics ($2f_0$, $3f_0$, etc.). The presence of these frequency peaks in a power spectrum corresponding to the spot mode indicates that the spot-to-plume transition is already promoted for this current value. This confirmed that the transition from spot mode to plume mode occurs continuously[37] as the discharge current increases or the mass flow rate decreases. If the discharge current is increased, the discharge mode will turn into plume mode. For every test case performed with the discharge in the spot mode, the overall aspect of the power spectrum is a low energy flat spectrum, with highly narrow peaks if the spot-to-plume transition occurs. For higher values of I_e, the discharge turns into plume mode and the power spectrum is greatly modified. The first dramatic change is due to the increased energy of the power spectrum. The average energy level of the spectrum corresponding to the plume mode is a few orders of magnitude greater in comparison with the spot mode. The second modification is that the narrow peaks detected in spot mode are replaced by broader peaks clearly visible in the power spectrum (both the fundamental and its harmonics).

For the discharge operated in plume mode, the fundamental frequencies detected range between 50 kHz and 90 kHz. Our measurements of f_0 match the frequency range that is generally reported in the literature for plume-mode oscillations of HT cathodes operated in diode configuration.[37–39] The fundamental frequency increases as the discharge current increases or the mass flow rate decreases.[28] Such a behavior is related to a modification of the plasma parameters.[23,37] The oscillations detected corresponds to medium-frequency oscillations ($\approx 40 - 200\,\mathrm{kHz}$) that are associated with IAI.[37,39] These oscillations can be related to two-stream (e-i) instability (Buneman instability) or IAI, depending on the plasma parameters.[23] Mikellides and co-workers[17,23] demonstrated that current-driven instabilities are responsible for the enhanced resistivity and nonclassical plasma transport in HT cathodes operated in diode configuration.

C. Temperatures

Figure 14 shows the steady-state temperatures measured with the thermocouples. Data for each mass flow rate are plotted versus the discharge current. At each current increment, the temperatures were allowed to reach steady state. In order to easily compare the different cases ($0.2\,\mathrm{mg\,s^{-1}}$, $0.4\,\mathrm{mg\,s^{-1}}$, and $0.6\,\mathrm{mg\,s^{-1}}$), a temperature offset of a few °C (positive or negative) is applied to the cases with $0.2\,\mathrm{mg\,s^{-1}}$ and $0.6\,\mathrm{mg\,s^{-1}}$ of Xe, equalizing the temperatures at $I_e = 2\,\mathrm{A}$. The errors bars in Fig. 14 correspond to the total uncertainties.[28]

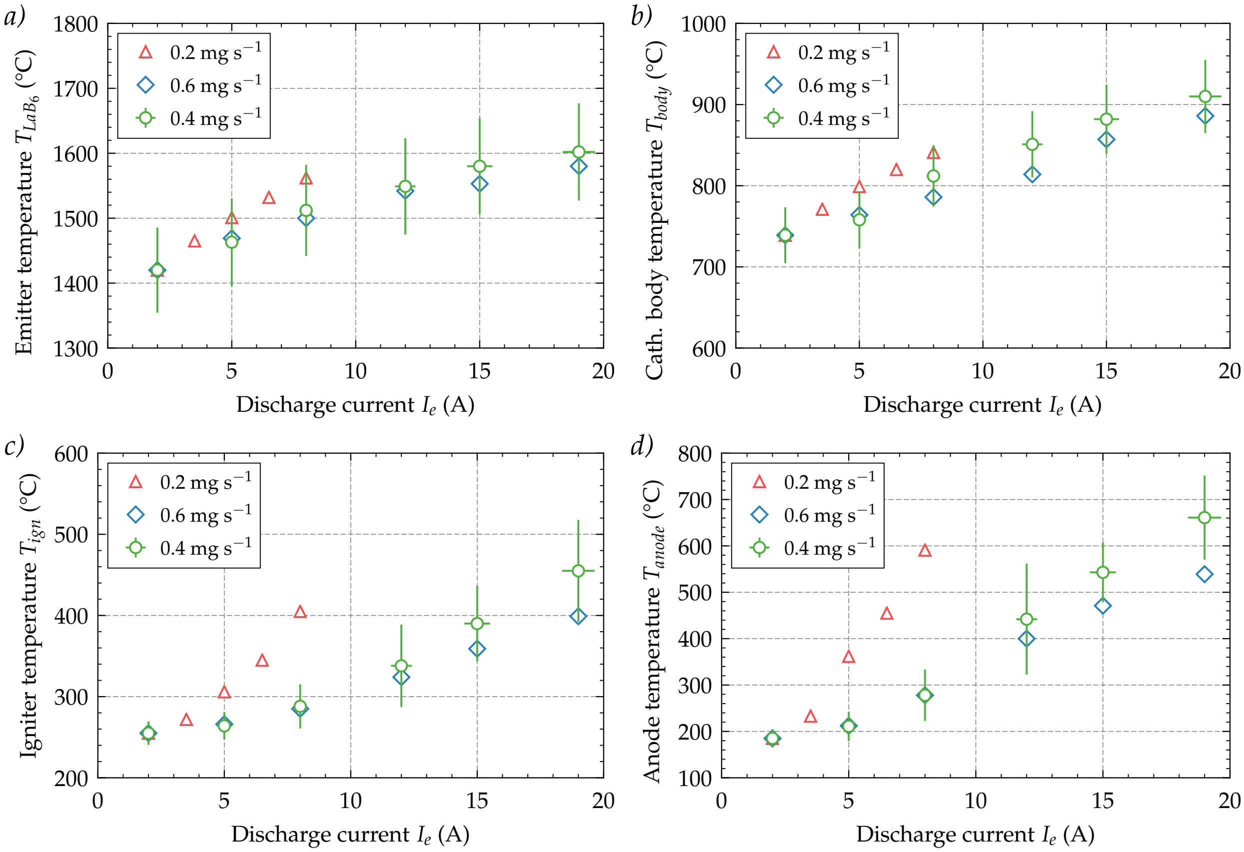

Figure 14. Temperature measurements during cathode operation of: *a)* emitter temperature (T_{LaB_6}), *b)* external body of the cathode (T_{boby}), *c)* igniter temperature (T_{ign}), and *a)* anode temperature (T_{anode}). For clarity, only the error bars of the $4\,\mathrm{mg\,s^{-1}}$-case are shown.

As expected, the higher the discharge current, the higher the temperature, whatever the measurement position. This phenomenon is explained by the higher energy that is transferred to the system when the current increases. In particular, the emitter temperature exhibits a clear increasing trend with the discharge current (Fig. 14a). This behavior is typical of HT cathodes and has been reported in the literature, including indirect (for BaO insert[36,40,41]) and direct (for BaO[26] and LaB_6[25] inserts) measurements with thermocouples of the emitter temperature during cathode operation. As previously observed, the case with a mass flow rate of $0.2\,\mathrm{mg\,s^{-1}}$ differs from the other two. The temperature trends with the discharge current are similar but the slopes are much higher than those with $0.4\,\mathrm{mg\,s^{-1}}$ and $0.6\,\mathrm{mg\,s^{-1}}$. The temperatures measured for this case are always the highest at a given value for the discharge current, including the temperature of the LaB_6 pellet. As concluded in the previous part, a mass flow rate of $0.2\,\mathrm{mg\,s^{-1}}$ of Xe is the worst case tested to operate the cathode in decent conditions, since the high insert temperature will lead to a decreased lifetime of the cathode[40] (due to the higher evaporation rate of the LaB_6 insert).

Whatever the measurement position considered, the onset of the plume mode does not induce a dramatic change in the temperature trend with the discharge current. This is relevant to the behavior reported in the literature for the orifice plate temperature.[36] One can observe that the temperatures of the emitter and other parts of the cathode decrease slightly with increasing flow rate (from $0.4\,\mathrm{mg\,s^{-1}}$ to $0.6\,\mathrm{mg\,s^{-1}}$). The decrease in the insert temperature with the mass flow rate was reported for a BaO-W insert[42] and LaB_6 insert,[25] for low-current operation (less than 20 A, typically). However, this trend is expected to reverse (*i.e.*, higher insert temperature for higher mass flow rates) for higher discharge current.[25,26] The same phenomenon is also expected to occur for the other parts of the cathode when the discharge current increases.[40]

In our cathode design, a low mass flow rate means that the plume mode is present. This results in an additional heating of the external body of the cathode due to the energetic ions returning onto this part of the cathode (see Sect. IV). In addition, the plume mode is also responsible for a higher heating of the anode due to the collection of electrons that are more energetic[8] (see Sect. IV). In return, supplementary heat fluxes are radiated from the anode and the inside face of the external body, both contributing to the overheating of the LaB_6 pellet measured when the mass flow rate is low. This assumption is supported by the fact that the temperature difference for the anode between 0.4 mg s^{-1} and 0.6 mg s^{-1} is higher than the one calculated for the LaB_6 pellet temperature.

Several work functions and values of the emission coefficients (*i.e.*, ϕ and A or D^4) have been reported in the literature for LaB_6, depending on the measurement method of the emission coefficients, temperature range of the measurement, surface stoichiometry (La-to-B ratio), and crystal structure (single-crystal or polycrystalline emitter), to name a few factors. Table 2 shows the emission coefficients used to plot the estimated temperature in Fig. 15. It can be seen that Table 2 presents some references[22,43–45] suggested in the extensive work of Goebel and co-workers.[4] These references are frequently cited by many other research teams in the context of LaB_6 HT cathodes. In addition, Table 2 also introduces three less-cited sets of emission coefficients.[46–48] One can observe on Fig. 15 that a given value for the emission current density can be obtained within a temperature range of about 300 °C, depending on what set of emission coefficients is considered.

Table 2. Work function ϕ and Richardson coefficient A (or D^4) of sintered LaB_6.

From	ϕ (eV)	A (A cm^{-2} K^{-2})	Temp. range (°C)	Comment
Ref. 22	2.66	29	750-1000	
Ref. 46	2.68	73	1500	
Ref. 43	2.66+1.23e^{-4}T	120	750-1000	Ref. 22, T in K
Ref. 47	2.40	40	1450-1650	
Ref. 44	2.87	110	900-1150	$LaB_{6.01}$
Ref. 45	2.91	120	1200-1400	
Ref. 48	2.36	120	750-1050	38% porosity

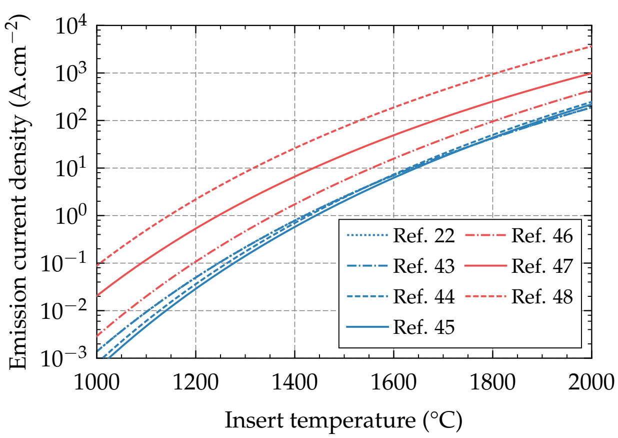

Figure 15. Emission current density calculated with Eq. (1) and emission coefficients from Table 2 according to the insert temperature.

Figure 16a shows the emitter temperature for the mass flow rate of 0.4 mg s^{-1} of Xe (open circles) and the temperature estimated from the Richardson-Dushman equation (thermionic emission) for different LaB_6 materials found in the literature (curves), versus the current. The current for the experimental data corresponds to the measured value of the discharge current I_e. The contribution of the bulk ionization to the total current is therefore neglected here, even though it accounts for a certain part of the total current (see Sect. IV). The ratio of the electron current emitted at the pellet to the total current depends indeed on the cathode geometry,[49] the insert material,[50] and the operating conditions.[50,51] The curves plotted in Fig. 16a correspond to the temperature calculated with Eq. (1), using the emission coefficients of Table 2 and a current density calculated with an electron emission surface of $0.283\,\text{cm}^2$ ($\pi \times 0.3\,\text{cm}^2$).

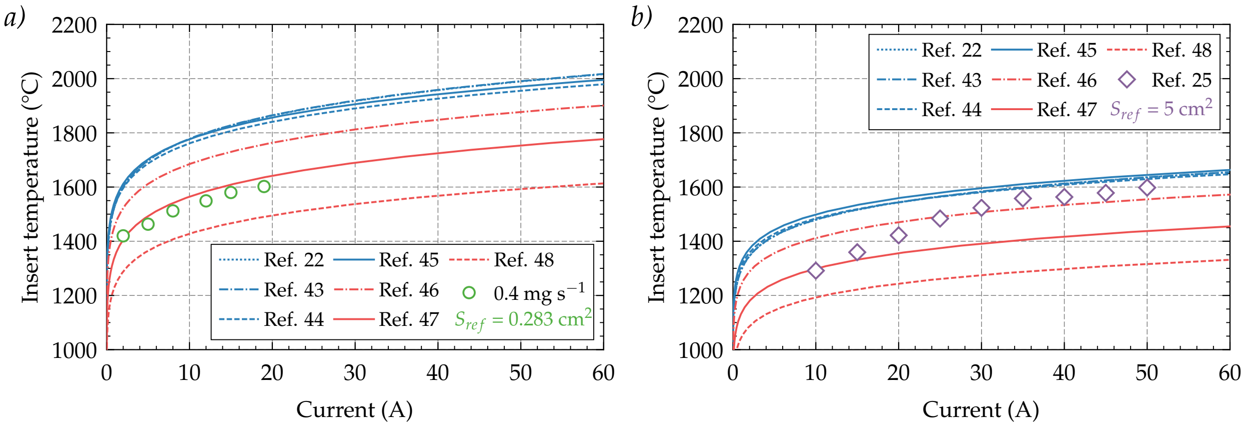

Figure 16. Comparison of the experimental data (open symbols) of the LaB_6 insert temperature and the estimated temperature from the Richardson-Dushman equation (curves), using the emission coefficients in Table 2 and the electron emission surface S_{ref}: *a)* experimental case with $0.4\,\text{mg}\,\text{s}^{-1}$ of Xe, present study ($S_{ref} = 0.283\,\text{cm}^2$), and *b)* data from Ref. 25 (case with $13\,\text{sccm}$ of Xe, $S_{ref} = 5\,\text{cm}^2$).

One can observe in Fig. 16a that experimental data (open symbols) are significantly lower than temperatures estimated with the Richardson-Dushman equation and the emission coefficients generally used in the studies dedicated to LaB_6 HT cathodes[4] ($2.66\,\text{eV} < \phi < 2.91\,\text{eV}$, see Table 2). Such a difference between temperature measurements and emission curves have been reported recently for a high-current cathode with a cylindrical LaB_6 insert,[25] for value of the discharge current lower than $\approx 20\,\text{A}$ (Fig. 16b). This discrepancy is therefore not surprisingly and several phenomena can be considered to explain the lower-than-expected temperature values:

- temperature measurement of the LaB_6 insert: in our cathode design, an underestimation of the insert temperature can be due to the positioning of the thermocouple tip.[28]
- cathode design: a radial gradient of the insert temperature may be present during the cathode operation, since the LaB_6 has a flat disk shape. In the case of a cylindrical shape, the temperature gradient occurs along the insert.[25]
- ratio of the emission current at the insert to the total current: in HT cathodes, several sources contribute to the discharge current, including the thermionic electrons from the insert and the ions from the plasma. The discharge current measured experimentally is therefore different to the emission current at the insert (see Sect. IV).
- plasma effects: as pointed out in a recent experimental study,[25] the effective work function must be lower than the work function value taken from the literature to explain the discrepancies observed between experimental data and empirical curves. Plasma effects, such as Schottky effect and space charge effect, occur indeed during operation of HT cathodes and can modify the effective value of the work function.[15,17] The Schottky-enhanced emission in HT cathodes is supported by a recent numerical study,[16] showing that a work function reduction of about $0.1\,\text{eV}$ ($\approx 5\%$) can occur in the case of a cathode with a BaO-W cylindrical insert. In our design, numerical simulations have shown that plasma effects can induce a few % reduction of the work function (see Sect. IV).
- work function measurement: the uncertainty of the work function may also play a role in the discrepancy between experimental data and emission curves. An uncertainty of $\pm 5\%$ on the LaB_6 work function induces an uncertainty of $\pm 150\,°\text{C}$ on the insert temperature.[28]

- emission coefficients: if a different set of emission coefficients is considered, for instance those of Ref. 47, the discrepancy between experimental data and empirical curves can be greatly reduced.[28] The emission coefficients taken from the literature may not be sufficiently characteristic of the LaB_6 material used in the tested cathode. In addition, the temperature range considered to measure the work function may play a role on the estimated value of the work function. For instance, the work function of Ref. 22 has been determined over the 750 °C − 1000 °C temperature range, whereas the work function of Ref. 47 was measured over the 1450 °C − 1650 °C temperature range. Therefore, it would be better to measure the emission coefficients of the same LaB_6 material as the one used in the HT cathode, in experimental conditions close to the ones occurring during the cathode operation, rather than using a set of emission coefficients taken from the literature.

VII. Conclusion

In this paper we have examined the operation of a cathode in a diode mode based on an alternative geometry to the traditional tubular emissive cathode geometries. The emitter is here a pellet placed face to the orifice whose temperature has been measured experimentally. The cathode operates in a non self-heating mode, the high emitter temperature at the surface of the pellet being sustained with an external heater system. This simplifies the modeling of the cathode operation since a thermal model of the cathode, which limits the predictive aspect of the simulations, is not needed. The simulations have been realized for two operating points (for a discharge current set at 4.8 A then 12 A). We have analyzed in details both the inner part of the cathode (where emission takes place) as well as the plume. In particular, it was possible to show by simulation the presence of plasma instabilities in the plume of the cathode when a strong discharge current is applied leading to periodic oscillations of plasma properties. Experimentally, the high current operating point is characterized by an intense light emission downstream of the cathode orifice (plume mode), which is confirmed qualitatively by the simulation results.

Acknowledgments

This work is supported by the CNES Direction des Lanceurs Research and Technology Program. R. Joussot benefits from a CNES post-doctoral fellowship and a financial support from Safran. G. Sary has benefited from a CNES-Safran Ph.D. Grant. L. Grimaud benefits from a CNES-Région Centre Ph.D. Grant.

References

[1]Goebel, D. M. and Katz, I., *Fundamentals of electric propulsion: ion and Hall thrusters*, John Wiley & Sons, Hoboken (NJ), 2008.

[2]Guerrini, G., Vesselovzorov, A. N., Bacal, S., and Pokrovsky, I. B., "Investigation of a small, closed electron drift, stationary plasma thruster," *Rev. Sci. Instrum.*, Vol. 67, No. 3, 1996, pp. 990–2, doi: 10.1063/1.1146793.

[3]Sengupta, A., "Destructive physical analysis of hollow cathodes from the Deep Space 1 flight spare ion engine 30,000 hr life test," *29th International Electric Propulsion Conference, Princeton (NJ), U.S.A., 31 October-4 November, 2005, IEPC-2005-026*, 2005, pp. 1–17, link.

[4]Goebel, D. M., Watkins, R. M., and Jameson, K. K., "LaB_6 hollow cathodes for ion and Hall thrusters," *J. Propul. Power*, Vol. 23, No. 3, 2007, pp. 552–8, doi: 10.2514/1.25475.

[5]Chu, E. and Goebel, D. M., "High-current lanthanum hexaboride hollow cathode for 10-to-50-kW Hall thrusters," *IEEE Transactions on Plasma Sciences*, Vol. 40, No. 9, 2012, pp. 2133–44, doi: 10.1109/TPS.2012.2206832.

[6]Pedrini, D., Albertoni, R., Paganucci, F., and Andrenucci, M., "Experimental Characterization of a Lanthanum Hexaboride Hollow Cathode for Five-Kilowatt-Class Hall Thrusters," *J. Propul. Power*, Vol. 32, No. 6, 2016, pp. 1557–61, doi: 10.2514/1.B35828.

[7]Kubota, K., Oshio, Y., Watanabe, H., Cho, S., Ohkawa, Y., and Funaki, I., "Numerical and Experimental Study on Discharge Characteristics of High-Current Hollow Cathode," *52nd AIAA/SAE/ASEE Joint Propulsion Conference, Salt Lake City (UT), U.S.A., July 25-27, 2016, AIAA 2016-4628*, 2016, pp. 1–9, doi: 10.2514/6.2016-4628.

[8]Domonkos, M. T., *Evaluation of Low-Current Orificed Hollow Cathodes*, Ph.D. thesis, University of Michigan, U.S.A., 1999.

[9]Touzeau, M., Prioul, M., Roche, S., Gascon, N., Pérot, C., Darnon, F., Béchu, S., Philippe-Kadlec, C., Magne, L., Lasgorceix, P., Pagnon, D., Bouchoule, A., and Dudeck, M., "Plasma diagnostic systems for Hall-effect plasma thrusters," *Plasma Phys. Contr. F.*, Vol. 42, No. 12B, 2000, pp. B323, doi: 10.1088/0741-3335/42/12B/324.

[10]Albarède, L., Lago, V., Lasgorceix, P., Dudeck, M., Bugrova, A. I., and Malik, K., "Interaction of a hollow cathode stream with a Hall thruster," *28th International Electric Propulsion Conference, Toulouse, France, March 17-21, 2003, IEPC-2003-333*, 2003, pp. 1–18, link.

[11]Albarède, L., *Etudes expérimentales d'un propulseur à effet Hall - Comportement stationnaire et dynamique du flux d'électrons*, Ph.D. thesis, Université d'Orléans, France, 2004, in French.

[12]Makela, J. M., Massey, D. R., and King, L. B., "Bismuth Hollow Cathode for Hall Thrusters," *J. Propul. Power*, Vol. 24, No. 1, 2008, pp. 142–6, doi: 10.2514/1.29389.

[13]Ning, Z., Yu, D., Li, H., and Yan, G., "Effect of the hollow cathode heat power on the performance of an Hall-effect thruster," *Plasma Sci. Technol.*, Vol. 11, No. 2, 2009, pp. 194–9, doi: 10.1088/1009-0630/11/2/12.

[14]Grimaud, L., Pétin, A., Vaudolon, J., and Mazouffre, S., "Perturbations induced by electrostatic probe in the discharge of Hall thrusters," *Rev. Sci. Instrum.*, Vol. 87, No. 4, 2016, pp. 043506, doi: 10.1063/1.4945563.

[15]Sary, G., Garrigues, L., and Boeuf, J.-P., "Hollow cathode modeling: I. A coupled plasma thermal two-dimensional model," *Plasma Sources Sci. T.*, Vol. 26, No. 5, 2017, pp. 055007, doi: 10.1088/1361-6595/aa6217.

[16]Sary, G., Garrigues, L., and Boeuf, J.-P., "Hollow cathode modeling: II. Physical analysis and parametric study," *Plasma Sources Sci. T.*, Vol. 26, No. 5, 2017, pp. 055008, doi: 10.1088/1361-6595/aa6210.

[17]Mikellides, I. G., Katz, I., Goebel, D. M., and Polk, J. E., "Hollow cathode theory and experiment. II. A two-dimensional theoretical model of the emitter region," *J. Appl. Phys.*, Vol. 98, No. 11, 2005, pp. 113303, doi: 10.1063/1.2135409.

[18]Mikellides, I. G., Goebel, D. M., Snyder, J. S., Katz, I., and Herman, D. A., "The discharge plasma in ion engine neutralizers: Numerical simulations and comparisons with laboratory data," *J. Appl. Phys.*, Vol. 108, No. 11, 2010, pp. 113308, doi: 10.1063/1.3514560.

[19]Mikellides, I. G., Goebel, D. M., Jorns, B. A., Polk, J. E., and Guerrero, P., "Numerical simulations of the partially ionized gas in a 100-A LaB_6 hollow cathode," *IEEE Transactions on Plasma Science*, Vol. 43, No. 1, 2015, pp. 173–84, doi: 10.1109/TPS.2014.2320876.

[20]Lieberman, M. A. and Lichtenberg, A. J., *Principles of plasma discharges and materials processing*, John Wiley & Sons, Hoboken (NJ), 2005.

[21]Lin, T. P. and Eng, G., "Thermionic emission including both space-charge and image forces," *J. Appl. Phys.*, Vol. 65, No. 8, 1989, pp. 3205–11, doi: 10.1063/1.342672.

[22]Lafferty, J. M., "Boride cathodes," *J. Appl. Phys.*, Vol. 22, No. 3, 1951, pp. 299–309, doi: 10.1063/1.1699946.

[23]Mikellides, I. G., Katz, I., Goebel, D. M., and Jameson, K. K., "Evidence of nonclassical plasma transport in hollow cathodes for electric propulsion," *J. Appl. Phys.*, Vol. 101, No. 6, 2007, pp. 063301, doi: 10.1063/1.2710763.

[24]Davidson, R. C. and Krall, N. A., "Anomalous transport in high-temperature plasmas with applications to solenoidal fusion systems," *Nuclear Fusion*, Vol. 17, No. 6, 1977, pp. 1313, doi: 10.1088/0029-5515/17/6/017.

[25]Polk, J. E., Goebel, D. M., and Guerrero, P., "Thermal Characteristics of a Lanthanum Hexaboride Hollow Cathode," *Joint Conference of 30th International Symposium on Space Technology and Science, 34th International Electric Propulsion Conference and 6th Nano-satellite Symposium, Hyogo-Kobe, Japan, July 4-10, 2015, IEPC-2015-44/ISTS-2015-b-44*, 2015, pp. 1–12, link.

[26]Coletti, M. and Gabriel, S. B., "Insert Temperature Measurements of a 180A Hollow Cathode for the HiPER Project," *48th AIAA/ASME/SAE/ASEE Joint Propulsion Conference & Exhibit, Atlanta (GA), U.S.A., 30 July-01 August, 2012, AIAA 2012-4081*, 2012, pp. 1–17, doi: 10.2514/6.2012-4081.

[27]Ohkawa, Y., Higuchi, T., Hayakawa, Y., Miyazaki, K., and Nagano, H., "Observation and Analysis of Graphite Hollow Cathode after 45,000-Hour Life Test," *33rd International Electric Propulsion Conference, Washington D.C., U.S.A., October 6-10, 2013, IEPC-2013-364*, 2013, pp. 1–9, link.

[28]Joussot, R., Grimaud, L., and Mazouffre, S., "Examination of a 5 A-class cathode with a LaB_6 flat disk emitter in the 2 A-20 A current range," *Vacuum*, Vol. 146, 2017, pp. 52–62, doi: 10.1016/j.vacuum.2017.09.021.

[29]Kaufman, H. R., "Technology of electron-bombardment ion thrusters," *Advances in Electronics and Electron Physics*, edited by L. Marton, Vol. 36, Academic Press, New York, 1974, pp. 265–373, doi: 10.1016/S0065-2539(08)61121-X.

[30]Mandell, M. J. and Katz, I., "Theory of Hollow Cathode Operation in Spot and Plume Modes," *30th Joint Propulsion Conference and Exhibit, Indianapolis (IN), U.S.A., June 27-29, 1994, AIAA-94-3134*, 1994, pp. 1–6, doi: 10.2514/6.1994-3134.

[31]Siegfried, D. E. and Wilbur, P. J., "An investigation of mercury hollow cathode phenomena," *13th International Electric Propulsion Conference, San Diego (CA), U.S.A., April 25-27, 1978, AIAA 1978-705*, 1978, pp. 1–11, doi: 10.2514/6.1978-705.

[32]Goebel, D. M. and Watkins, R. M., "LaB_6 Hollow Cathodes for Ion and Hall Thrusters," *41st AIAA/ASME/SAE/ASEE Joint Propulsion Conference & Exhibit, Tucson (AZ), U.S.A., July 10-13, 2005, AIAA 2005-4239*, 2005, pp. 1–9, doi: 10.2514/6.2005-4239.

[33]Vekselman, V., Krasik, Y. E., Gleizer, S., Gurovich, V. T., Warshavsky, A., and Rabinovich, L., "Characterization of a Heaterless Hollow Cathode," *J. Propul. Power*, Vol. 29, No. 2, 2013, pp. 475–86, doi: 10.2514/1.B34628.

[34]Rehn, L. and Kaufman, H. R., "Correlation of Inert Gas Hollow Cathode Performance," *13th International Electric Propulsion Conference, San Diego (CA), U.S.A., April 25-27, 1978, AIAA 1978-707*, 1978, pp. 1–8, doi: 10.2514/6.1978-707.

[35]Sakai, S., Katayama, T., Aoyagi, J., and Takegahara, H., "Discharge Modes and Characteristics of Hollow Cathode," *30th International Electric Propulsion Conference, Florence, Italy, September 17-20, 2007, IEPC-2007-215*, 2007, pp. 1–7, link.

[36]Domonkos, M. T., Patterson, M. J., and Gallimore, A. D., "Low-Current, Xenon Orificed Hollow Cathode Performance for In-Space Applications," *J. Propul. Power*, Vol. 19, No. 3, 2003, pp. 438–43, doi: 10.2514/2.6127.

[37]Goebel, D. M., Jameson, K. K., Katz, I., and Mikellides, I. G., "Potential fluctuations and energetic ion production in hollow cathode discharges," *Phys. Plasmas*, Vol. 14, No. 10, 2007, pp. 103508, doi: 10.1063/1.2784460.

[38]Goebel, D. M., Jameson, K., Katz, I., Mikellides, I. G., and Polk, J., "Energetic ion production and keeper erosion in hollow cathode discharges," *29th International Electric Propulsion Conference, Princeton (NJ), U.S.A., 31 October-4 November, 2005, IEPC-2005-266*, 2005, pp. 1–18, link.

[39]Nishiyama, K., Shimizu, Y., Funaki, I., Kuninaka, H., and Toki, K., "Ground chamber measurements of the electromagnetic emissions from the Hayabusa ion engine," *J. Propul. Power*, Vol. 23, No. 3, 2007, pp. 513–21, doi: 10.2514/1.19473.

[40]Kamhawi, H. and Van Noord, J., "Development and Testing of High Current Hollow Cathodes for High Power Hall Thrusters," *48th AIAA/ASME/SAE/ASEE Joint Propulsion Conference & Exhibit, Atlanta (GA), U.S.A., 30 July-01 August, 2012, AIAA 2012-4080*, 2012, pp. 1–13, doi: 10.2514/6.2012-4080.

[41]Plasek, M. L., Wordingham, C. J., Roja Mata, S., Choueiri, E., and Polk, J. E., "Experimental Investigation of the RF-Controlled Hollow Cathode," *50th AIAA/ASME/SAE/ASEE Joint Propulsion Conference, Cleveland (OH), U.S.A., July 28-30, 2014, AIAA 2014-3825*, 2014, pp. 1–14, doi: 10.2514/6.2014-3825.

[42]Polk, J., Marrese, C., Thornber, B., Dang, L., and Johnson, L., "Temperature Distributions in Hollow Cathode Emitters," *40th AIAA/ASME/SAE/ASEE Joint Propulsion Conference and Exhibit, Fort Lauderdale (FL), U.S.A., July 11-14, 2004, AIAA 2004-4116*, 2004, pp. 1–17, doi: 10.2514/6.2004-4116.

[43]Kohl, W. H., *Handbook of materials and techniques for vacuum devices*, Van Nostrand Reinhold, New York, 1967.

[44]Jacobson, D. L. and Storms, E. K., "Work function measurement of lanthanum-boron compounds," *IEEE T. Plasma Sci.*, Vol. 6, No. 2, 1978, pp. 191–9, doi: 10.1109/TPS.1978.4317109.

[45]Storms, E. K. and Mueller, B., "Phase relationship, vaporization, and thermodynamic properties of the lanthanum-boron system," *J. Phys. Chem.-US*, Vol. 82, No. 1, 1978, pp. 51–9, doi: 10.1021/j100490a014.

[46]Kudintseva, G. A. and Tsarev, B. M., "Emission properties of hexaborides of certain rare-earth metals," *Radiotekhnika I Elektronika*, Vol. 3, 1958, pp. 428–29.

[47]Ahmed, H. and Broers, A. N., "Lanthanum hexaboride electron emitter," *J. Appl. Phys.*, Vol. 43, No. 5, 1972, pp. 2185–92, doi: 10.1063/1.1661472.

[48]Pelletier, J. and Pomot, C., "Work function of sintered lanthanum hexaboride," *Appl. Phys. Lett.*, Vol. 34, No. 4, 1979, pp. 249–51, doi: 10.1063/1.90769.

[49]Sary, G., *Modélisation d'une cathode creuse pour propulseur à plasma*, Ph.D. thesis, Université de Toulouse, Université Toulouse III-Paul Sabatier, France, 2016.

[50]Sary, G., Garrigues, L., and Boeuf, J.-P., "Hollow cathode modeling: a first approach on scaling laws," *Joint Conference of 30th International Symposium on Space Technology and Science, 34th International Electric Propulsion Conference and 6th Nano-satellite Symposium, Hyogo-Kobe, Japan, July 4-10, 2015, IEPC-2015-14/ISTS-2015-b-14*, 2015, pp. 1–15, link.

[51]Mikellides, I. G., Katz, I., Goebel, D. M., Polk, J. E., and Jameson, K. K., "Plasma processes inside dispenser hollow cathodes," *Phys. Plasmas*, Vol. 13, No. 6, 2006, pp. 063504, doi: 10.1063/1.2208292.